

Article

Effect of Composition on Engineering Behavior of Clay Tills

Rajeevkar Paranthaman  and Shahid Azam * 

Environmental Systems Engineering, Faculty of Engineering and Applied Science, University of Regina, Regina, SK S4S 0A2, Canada; rpt959@uregina.ca

* Correspondence: shahid.azam@uregina.ca

Abstract: Glacial geology, marine environment, and arid climate govern the composition of clay tills. The main purpose of this work is to develop a clear understanding of the engineering behavior of compacted clay till under soil suction and applied stress. The results indicate moderate water adsorption due to the presence of clay minerals (26% corrensite, 10% illite, and 8% kaolinite) with Ca^{2+} as the dominant cation and a flocculated fabric in a slightly basic ($\text{pH} = 7.5$) pore water. The water retention curve comprised four transition points that are associated with capillary water drainage from large pores (air entry value of 2 kPa and residual suction value of 20 kPa) and small pores (air entry value of 700 kPa and residual suction value of 5×10^4 kPa). Beyond the last value, vapor flow is dominant and removes the adsorbed water by evaporation. The ratio of soil volume change to water volume change best described the s-shaped shrinkage path that also comprised four stages, namely: from most large pores with low volume change; from remaining large and most small pores along with almost equal volume change; from some small pores with low volume change; and from the rest of the small pores with no volume change. Likewise, the s-shaped swelling potential curve comprised three stages and correlated well with bimodal hydraulic conductivity curve, that is, slow initial swelling (unsaturated hydraulic conductivity around 10^{-14} m/s) due to expansion of peripheral clay in lumps; high primary swelling (unsaturated hydraulic conductivity of up to 10^{-11} m/s) due to thickened double layer of most colloids; and slow secondary swelling (albeit unsaturated hydraulic conductivity around 10^{-10} m/s) due to expansion of remaining particles. Soil compression (compression index of 0.164) was due to a gradual reduction in number of large pores, whereas rebound (swelling index of 0.047) was due to water adsorption on clay with part of the deformations recovered. Finally, the consolidation rate was related to saturated hydraulic conductivity, which varied by three orders of magnitude.

Keywords: clay tills; soil composition; water retention; volume change; hydraulic conductivity



Citation: Paranthaman, R.; Azam, S. Effect of Composition on Engineering Behavior of Clay Tills. *Geosciences* **2021**, *11*, 427. <https://doi.org/10.3390/geosciences11100427>

Academic Editors: Hadi Khabbaz, Roger Urgeles Esclasans and Jesus Martinez-Frias

Received: 21 July 2021

Accepted: 4 October 2021

Published: 15 October 2021

Publisher's Note: MDPI stays neutral with regard to jurisdictional claims in published maps and institutional affiliations.



Copyright: © 2021 by the authors. Licensee MDPI, Basel, Switzerland. This article is an open access article distributed under the terms and conditions of the Creative Commons Attribution (CC BY) license (<https://creativecommons.org/licenses/by/4.0/>).

1. Introduction

Clay tills are frequently encountered across the Northern Hemisphere, primarily in Canada, United Kingdom, Russia, Norway, Ireland, and Poland. These soils are heterogeneous mixtures of unsorted earth materials containing variable amounts of clays [1–3]. The presence of clay minerals governs the engineering behavior of such soils, owing to water adsorption and retention. The resulting flow through and volumetric changes have been reported to severely affect the integrity of civil infrastructure. For example, 18 month construction halt due to low hydraulic conductivity and high pore pressures in Alameda dam extension (Saskatchewan, Canada) [4] and post-construction settlement of 900 mm in Saint-Marguerite–3 dam partly due to consolidation (Quebec, Canada) [5]. Generally, the behavior of earth structures is related to the following: seasonal weather causing saturation–desaturation and resulting in alternate swelling and shrinkage [6,7] and construction loading causing initial pore pressure increase and subsequent settlement [8,9]. Given that several new large-scale projects (such as irrigation canals from Diefenbaker Lake and Pike Lake and rehabilitation of Gardiner dam) have to be constructed from local clay tills, there is a need to understand flow through and volumetric changes in such soils.

The engineering characteristics of clayey soils are governed by specific minerals (smectite, illite, and kaolinite) possessing small particles and high cation exchange [10]. Their behavior can be described by the stress state variables of soil suction due to precipitation and evaporation and applied stress due to overburden or structural load. Suction is generated by capillary action at the air–water interface in soil pores and water adsorption by clay mineral surfaces through diffuse double layer interactions. Both mechanisms restrict water movement such that capillarity (driven by matric potential) is operative at low suction [11,12] and adsorption (driven by electrical potential) is dominant at high suction [13,14]. Swelling of an initially dry soil (high suction) occurs due to hydration of clay particle surfaces forming thin water films (diffuse double layers (1 nm to 100 nm)) by van der Waals attraction [10,15]. These water films gradually increase in size (8 nm to 680 nm [16]) thereby developing water menisci in the soil pores and decrease suction that diminishes at full saturation [17,18]. The reverse order of water expulsion has been observed during shrinkage of an initially wet soil [19]. Likewise, consolidation of an initially saturated soil occurs by the expulsion of pore water, whereas the adsorbed water remains attached to clay minerals [20]. Furthermore, the hydraulic conductivity under a given stress state determines the rate at which volumetric changes take place. Such interrelated phenomena require a fundamental understanding of mineral composition in conjunction with flow through, swell-shrink, and compression-rebound.

The main objective of this paper was to investigate the effect of composition on the engineering behavior of clay tills. First, index properties were determined for preliminary soil assessment. Second, mineral and water compositions were determined to appreciate the geological origin and water adsorption of the clay till. Third, the water retention curve (WRC) was determined along with the shrinkage curve (SC) to understand the water holding capacity during volume changes under soil suction. Fourth, the swell-consolidation behavior was determined along with the hydraulic conductivity curve (HCC) to assess volume changes under applied stresses.

2. Geological Setting

Saskatchewan resides on sedimentary rocks from the Cretaceous to the Tertiary. These rocks developed due to tectonic activity that resulted in the rising of the Rocky Mountains and down-warping of the Williston Basin [21,22]. Physical weathering resulted in the accumulation of unsorted materials in the depression [23], whereas volcanic ash from eruptions in southwestern Montana deposited feldspar minerals in the region [24]. During the late Cretaceous period, the Western Interior Seaway (east of the Rocky Mountains from the Gulf of Mexico to the Arctic Ocean) was formed due to sea level rise [25]. Alternate sea level fluctuations caused physical and chemical weathering of the mountains thereby growing surficial materials as well as precipitating Na^+ , K^+ , Ca^{2+} , Mg^{2+} , Cl^- , CO_3^{2-} , and SO_4^{2-} as salts such as carbonates [26]. During the Tertiary period, rivers and channels originated from the Rocky Mountains and further deposited alluvial sediments [27]. Furthermore, the region experienced several periods of hot and dry climate from the Cretaceous to the Tertiary period [28,29]. This means that the basin facilitated the conversion of feldspars to clays because of marine environment, arid climate, and restrained leaching along with deposition of calcites and dolomites [30].

The region underwent extensive reworking due to multiple glacial events throughout the Quaternary period. Advancing ice sheets progressively scraped surficial materials and the retreating glacier deposited thick successions of clayey tills [2,31,32]. The present-day tills evolved in the predominantly flat geomorphology and semi-arid climate after the Wisconsinan 17,000 year BP through 11,000 years BP [33,34]. Based on stratigraphy and mean carbonate content, regional clay till formations include the following [35]: (i) the Sutherland group (60 m thick) has a carbonate content of 19 ± 8 mL CO_2/g and comprises the Mennon, Dundurn, and Warman formations; and (ii) the Saskatoon group (80 m thick) has a carbonate content of 34 ± 10 mL CO_2/g and comprises Floral and Battleford formations.

Figure 1 presents the plasticity chart developed by Cassagrande [36] with typical mineral ranges given by Holtz and Kovacs [37]. The data reported by Sauer et al. [3] indicated that most tills fall in the region designated as lean clay (CL). The liquid limit range for the Saskatoon group was 22% to 40%, whereas that for the Sutherland group was 35% to 52%. These data indicate that a low liquid limit is associated with high carbonate content (and vice versa), because the amount of adsorbed water on clay surfaces is reduced by the Ca^{2+} and Mg^{2+} ions in the carbonates. The behavior of both types of tills tends to be close to smectite clay minerals.

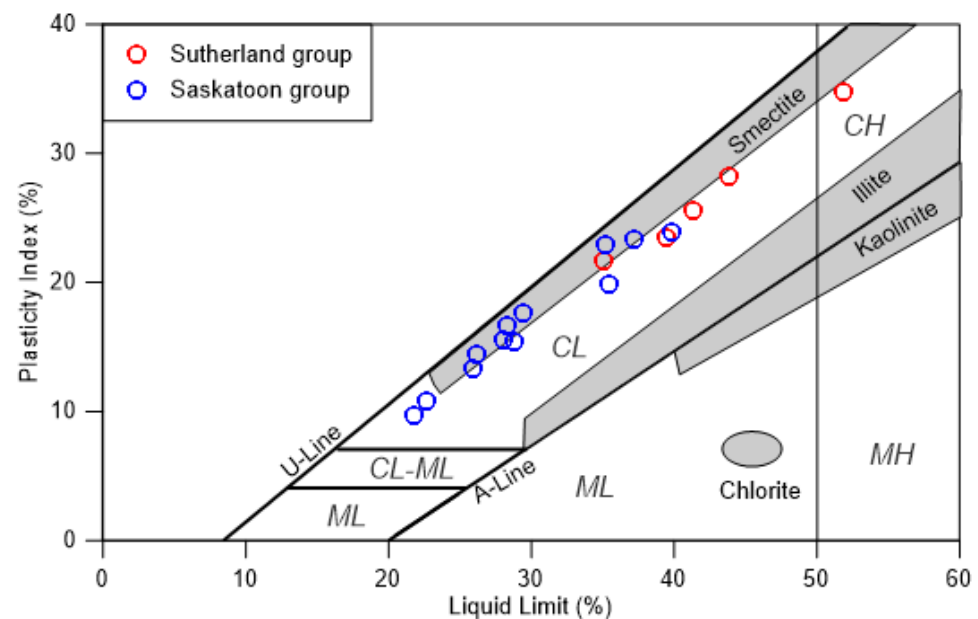


Figure 1. Plasticity chart showing clay tills in southern Saskatchewan (data from Sauer et al. [3]).

3. Research Methodology

The till samples were obtained from a surface deposit at Belle Plaine, Saskatchewan, Canada. The materials were collected in a 20 L bucket, sealed with polythene wrap to prevent water loss, and brought to the geoenvironmental laboratory at the University of Regina as per ASTM D4220/D4220M-14 [38]. The soil was air-dried at a temperature of 21 °C, the chunks were broken down, and visible coarse particles were removed. The remainder of the material was pulverized and the oversized (coarser than 4.75 mm) particles discarded. Pulverization was achieved by gently breaking down the material using a manual grinder to ensure that the natural sizes of the individual grains are not altered. The index properties were determined according to the following ASTM methods: (i) specific gravity (G_s) by ASTM D854-14 [39]; (ii) grain size distribution (GSD) by ASTM D422-63(2007) [40]; and (iii) liquid limit (w_l), plastic limit (w_p), and plasticity index (I_p) by ASTM D4318-17e1 [41]. The soil was classified using the ASTM D2487-17e1 [42]. The ASTM D2216-19 [43] was used for all soil properties requiring the determination of water content. This method uses oven drying of materials at 105 ± 5 °C, which does not affect the grain size distribution of sedimentary soils.

The mineral composition was determined by X-ray diffraction (XRD) analysis using a diffractometer (Bruker D4 Endeavor) equipped with a monochromatic incident beam (Co K-alpha) at 35 kV and 40 mA. To separate coarse particles from clay aggregates, a soil sample (2.5 g) finer than 0.075 mm was dispersed using sodium hexametaphosphate. The sample was centrifuged to separate coarse particles (coarser than 0.002 mm) at 600 rpm for 5 min and clay particles (finer than 0.002 mm) at 3000 rpm for 20 min. The coarse sample was air-dried at 22 °C, pulverized to a fine powder, mounted onto a glass slide with random particle orientation, and examined over an angle (2θ) of 4° to 75°. In contrast, preferentially oriented clay samples were prepared as follows: (i) in air-dried state to

develop the base case; (ii) ethylene glycol (EG) solvated to identify expansive clay minerals; and (iii) hydrochloric acid (HCl) solvated to identify soluble clay minerals. These samples were examined over an angle (2θ) of 4° to 50° . The Powder Diffraction File (PDF)-4 Mineral Database from the International Centre for Diffraction Data (ICDD) was used for mineral identification. Likewise, the reference intensity ratio (RIR) method was applied for mineral quantification [44].

Exchangeable cations were quantified through the inductively coupled plasma optical emission spectroscopy (ICP-OES). About 10 g of sample and 40 mL of 1 M ammonium acetate were added in a centrifuge tube that was agitated at 115 rpm for 5 min in a reciprocal shaker. The solution was re-agitated after 24 h for 15 min and filtered via Buchner funnel with a Whatman No.42 filter paper [45]. An extract from the filtered solution was placed in ICP-OES (Perkin Elmer Optima 7300s) to determine Na^+ , K^+ , Ca^{2+} , and Mg^{2+} . The sample was heated up to 7000°C and allowed to cool down. The cations were identified from the emitted light wavelengths and quantified from the spectroscopic intensity.

Thermo-gravimetric analysis (TGA) was conducted to understand weight loss due to soil water removal and mineral transitions. About 100 mg of powdered soil was placed in the analyzer (LECO TGA 701), and the temperature was raised from 28°C (ambient) to 950°C at a uniform rate of $2^\circ\text{C}/\text{min}$. To preclude oxidation, the analyzer was purged with nitrogen (N_2), and a gas flow of 7 L/min was maintained throughout the test.

The pore water characteristics were determined to assess the effect of clay–liquid interactions on soil fabric. A 1:1 slurry was prepared by mixing 50 g of material finer than 2 mm with 50 mL of distilled water. To separate material coarser than 0.002 mm, the slurry was centrifuged at 600 rpm for 5 min using Sorvall Thermo Scientific Biofuge Primo R. The pH and electrical conductivity (EC) were determined in accordance with ASTM D4972-19 [46] using OHAUS starter 2100 and ASTM D1125-14 [47] using EC meter (D-54), respectively. Likewise, zeta potential (ZP) was determined for a 1:1 slurry (with material finer 0.075 mm) using a Zeta Meter System 4.0. The sample preparation and measurement methods are described in Azam and Rima [48].

To understand the engineering behavior of constructed earthwork, the soil was compacted (water content, $w = 9\%$ and dry unit weight, $\gamma_d = 17 \text{ kN}/\text{m}^3$) according to ASTM D698-12e2 [49]. The WRC was determined following ASTM D6836-16 [50] using pressure extractors to apply selected suction (ψ) values: porous plate for up to 50 kPa and porous membrane for up to 2000 kPa. Several identical sub-samples (40 mm diameter and 10 mm thick) were cored from the compacted sample, placed on the respective plate or membrane, and allowed to saturate (achieved in up to four days) using distilled and de-aired water. The known suction value was applied and regularly monitored through the water level in a graduated burette that, in turn, was connected to the extractor. The test was stopped when successive readings over 24 h recorded an insignificant difference. Likewise, the dew point potentiometer (WP4-T) was utilized to measure suction beyond 2000 kPa. A sub-sample of about 8 g was trimmed from the compacted sample and put in the sampling cup that was subsequently placed in the potentiometer chamber. In the sealed chamber, water vapor pressure in the soil was equilibrated with air vapor pressure and suction readings were displayed on the screen. Equilibration time ranged from a few minutes for low suction to about one hour for high suction. In both methods, the water content was determined using ASTM D2216-19 [43].

The shrinkage curve was determined using two methods. The ASTM D4943-18 [51] standard was used for high water content (more than w_p). The sub-samples were obtained from the extractors after the termination of applied suction, and each was divided into two specimens for separate determination of water content (as before) and void ratio. To determine void ratio, one of the specimens with known mass was coated with molten microcrystalline wax ($G_s = 0.87$) and allowed to solidify. Thereafter, it was submerged in a water-filled beaker to determine the volume (equal to the displaced water volume) that, in turn, was duly corrected for wax volume. Likewise, a Vernier caliper was used to determine void ratio at low water content (less than w_p). A sub-sample (46 mm diameter and 18 mm

height) was cored from the compacted sample and allowed to desiccate. The changes in mass and volume were recorded at regular time intervals and used to calculate water content and void ratio, respectively.

The volume change characteristics were determined in two steps. Initially, free swelling was measured in accordance with the ASTM D4546-14e1 [52]. A sub-sample (63 mm diameter and 25 mm thick) was cored from the compacted sample, as before. The sub-sample was inundated under a seating pressure of 5 kPa and allowed to swell until consecutive readings in deformation over one week were found to be negligible. Thereafter, consolidation was carried out as per ASTM D2435/D2435M-11 [53] by applying incremental pressures. A digital camera was used to record the deformations readings of the dial gauge at specified time intervals. The test data were also analyzed to determine the saturated hydraulic conductivity (k_s) following the method described in Terzaghi et al. [54]. The k_s along with WRC was used to estimate HCC using empirical relationships.

4. Results and Discussion

4.1. Index Properties

Table 1 provides the geotechnical index properties of the clay till. The G_s was found to be 2.72, which is similar to that of clays. As shown in GSD (Figure 2), material finer than 0.075 mm measured 51% and that finer than 0.002 mm was 18%. The consistency limits ($w_l = 29\%$ and $w_p = 15\%$) indicated that the investigated till is similar to those in the Saskatoon group (Figure 1), which is a soil with moderate water retention and adsorption capacity. Using the plasticity chart, the corresponding shrinkage limit (w_s) was found to be 12%. The investigated soil was classified as lean clay (CL). These data are typical for clayey tills in the region [3].

Table 1. Summary of geotechnical index properties.

Soil Property	Value
Specific gravity, G_s	2.72
Material finer than 4.75 mm (%)	100
Material finer than 0.075 mm (%)	51
Material finer than 0.002 mm (%)	18
Liquid limit, w_l (%)	29
Plastic limit, w_p (%)	15
Shrinkage limit, w_s (%)	12
USCS symbol	CL

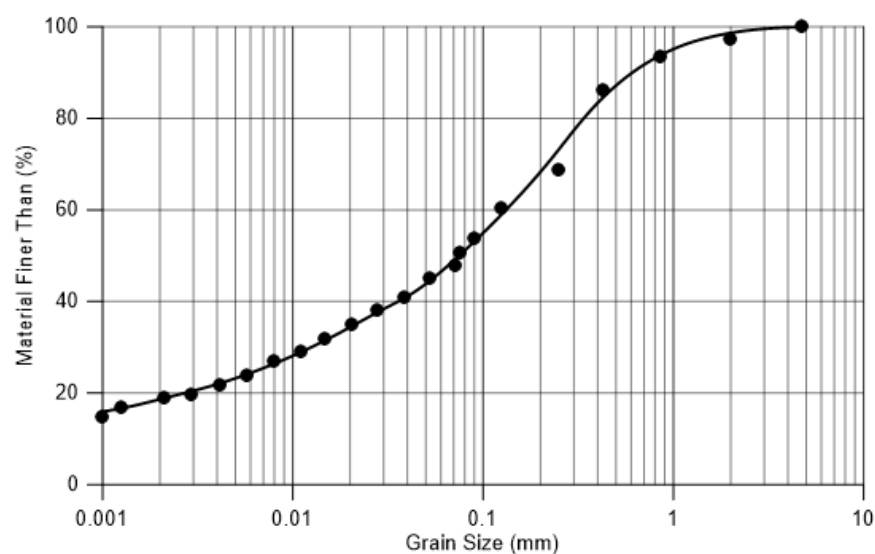
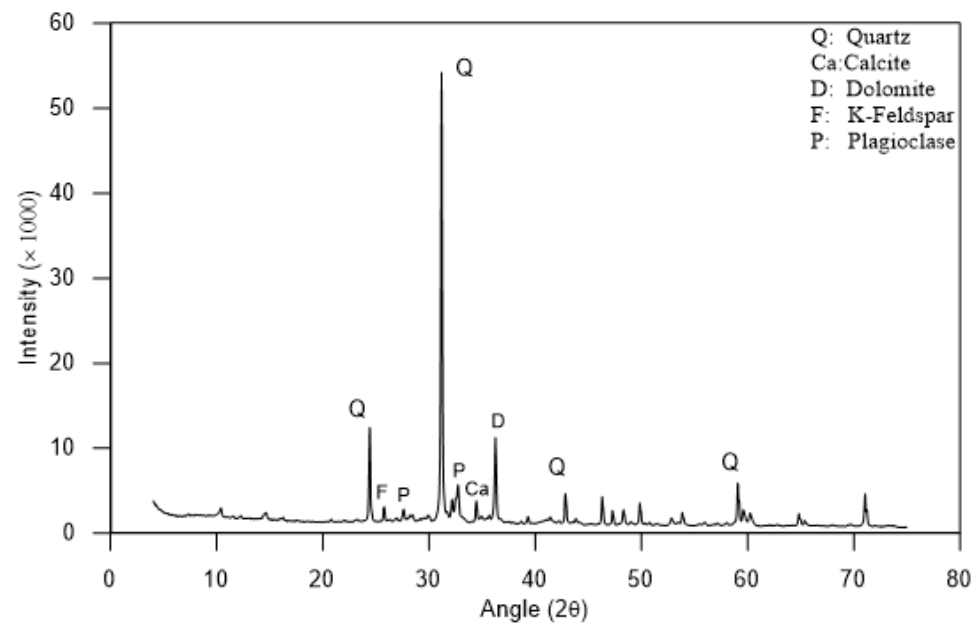


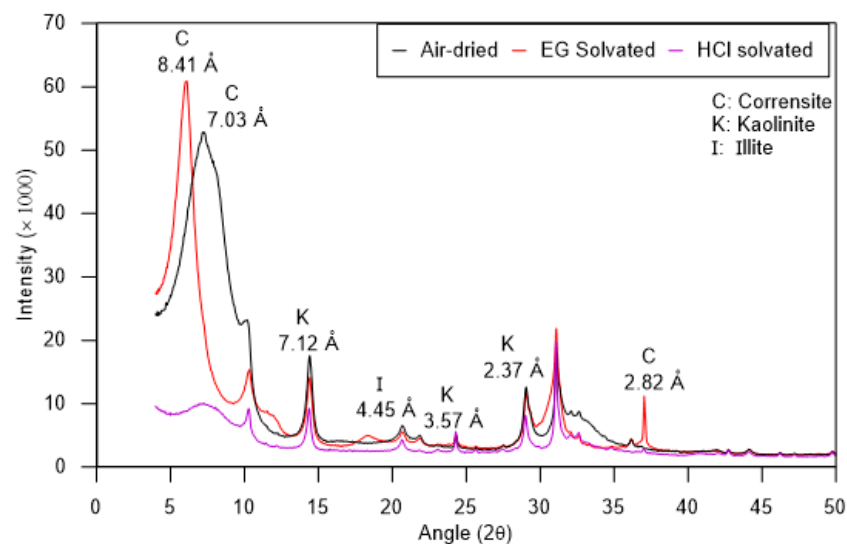
Figure 2. Grain size distribution of the investigated clay till.

4.2. Soil and Pore Water Compositions

Figure 3 plots the X-ray diffraction patterns of investigated clay till. The coarse sample (Figure 3a) showed quartz with diffraction peaks at 24.4° , 31.2° , 42.9° , and 59.1° . This validated the accuracy of the analyses for other minerals [10]. The existence of quartz indicated the sedimentary origin of the investigated till [55]. Likewise, calcite at 34.4° and dolomite at 36.3° in the sample are related to deposition of calcareous compounds from seawater [56]. Furthermore, various types of feldspars (K-feldspar at 25.8° and plagioclase at 27.7° and 32.7°) are related to the deposition of volcanic debris in the Cretaceous period and subsequent weathering during the Quaternary period.



(a)



(b)

Figure 3. X-ray diffraction patterns of investigated clay till: (a) coarse sample, (b) clay sample.

The clay sample (Figure 3b) showed the presence of corrensite (smectite–chlorite mixed layer) that generally forms during hydrothermal metamorphism occurs under low pressure and low temperature [57]. The occurrence of corrensite was confirmed from the following observations: (i) shift in peak of the basal spacing from 7.03 \AA (7.3° for air-dried

state) to 8.41 Å (6.10 for EG solvated); (ii) presence of a distinct peak at a basal spacing of 2.82 Å (37.0° for EG solvated); and (iii) absence of the first peak (HCl solvated) due to mineral decomposition [58]. In contrast, the presence of kaolinite (14.4°, 24.3°, and 29.1°) and illite (20.7°) were confirmed from the absence of shifts in peaks for EG solvated and HCl solvated samples.

Figure 4 gives the TGA results of the till in the form of total weight loss and weight loss rate. The sample exhibited a total weight loss of 11%. The weight loss rate curve shows two peaks with distinct weight reduction. The first peak existed between 28 °C and 190 °C with a weight loss of about 2% that corresponded to the removal of adsorbed water. The second peak occurred between 550 °C and 700 °C with a corresponding weight loss of about 5% due to the removal of hydroxyl ion [58].

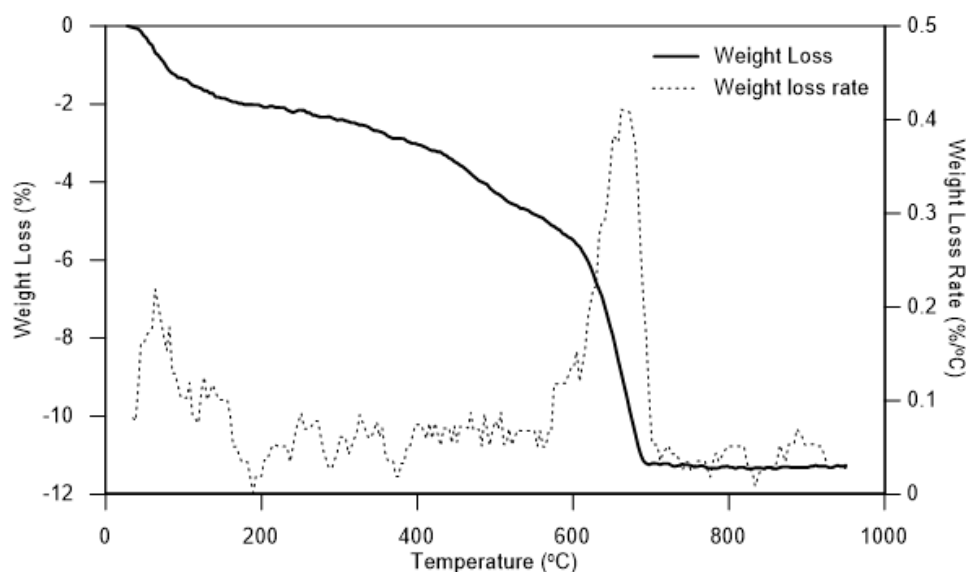


Figure 4. Thermo-gravimetric analysis of the investigated clay till.

Table 2 gives a summary of the mineralogical and pore water composition of the clay till. The clay till was found to contain 55% coarse minerals containing quartz (34%), dolomite (11%), and feldspars (6%) and 44% clay minerals constituting corrensite (26%), illite (10%), and kaolinite (8%). The total CEC of the sample was found to be 26.5 cmol(+)/kg. The presence of Ca²⁺ and Mg²⁺ is primarily related to the dissociation from dolomite whereas that of Na⁺ and K⁺ is associated with feldspars and clay minerals. These data indicate that the predominant exchange complex as Ca²⁺-corrensite that resulted in moderate water adsorption on the clay surfaces.

Table 2. Summary of soil and pore water compositions.

Property	Value
Minerals (%) *	Coarse (55) Quartz (34), Dolomite (11), Plagioclase (4), K-Feldspar (2), Calcite (2), Others (2)
	Clay (44) Corrensite (26), Illite (10), Kaolinite (8)
Exchangeable cations (cmol+)/kg	Na ⁺ (0.2), K ⁺ (0.9), Ca ²⁺ (19.1), Mg ²⁺ (6.2)
Total CEC (cmol+)/kg	26.5
pH	7.5
Electrical conductivity (µS/cm)	1725
Exchangeable sodium percentage (%) ^a	0.75
Zeta potential (mV)	-20.4

* Accuracy ± 1%. ^a ESP = $\frac{Na^+}{CEC} \times 100\%$.

The pore water was found to be slightly basic (pH = 7.5) with EC = 1725 μS/cm, which is in the range of clayey soils (100 to 10,000 μS/cm), as measured by Azam [59]. The exchangeable sodium percentage (ESP) was calculated to be 0.75%. This value is lower than 2% thereby indicating a flocculated fabric [10]. Similarly, ZP was measured to be −20.4 mV, which falls within the range of Ca²⁺ dominated clay minerals (−5 mV to −30 mV, as reported Chorom and Rengasamy [60]). The flocculated morphology is expected to affect the engineering behavior of the investigated clay [13].

4.3. Water Retention

Figure 5 gives the WRC for the investigated soil on a semi-logarithmic scale. The initial index properties ($w = 30\%$, $\theta = 42\%$, and $S = 98\%$) were plotted on the y -axis at an arbitrarily assigned low soil suction (0.1 kPa). The test data followed bimodal fits for w -based, θ -based, and S -based curves according to the following equation [61]:

$$w = w_s \left\{ \frac{s}{\left(\ln \left[2.718 + \left(\frac{a}{\psi} \right)^n \right] \right)^m} + \frac{1-s}{\left(\ln \left[2.718 + \left(\frac{j}{\psi} \right)^k \right] \right)^l} \right\} \left\{ 1 - \frac{\ln \left(1 + \frac{\psi}{3000} \right)}{5.812} \right\} \quad (1)$$

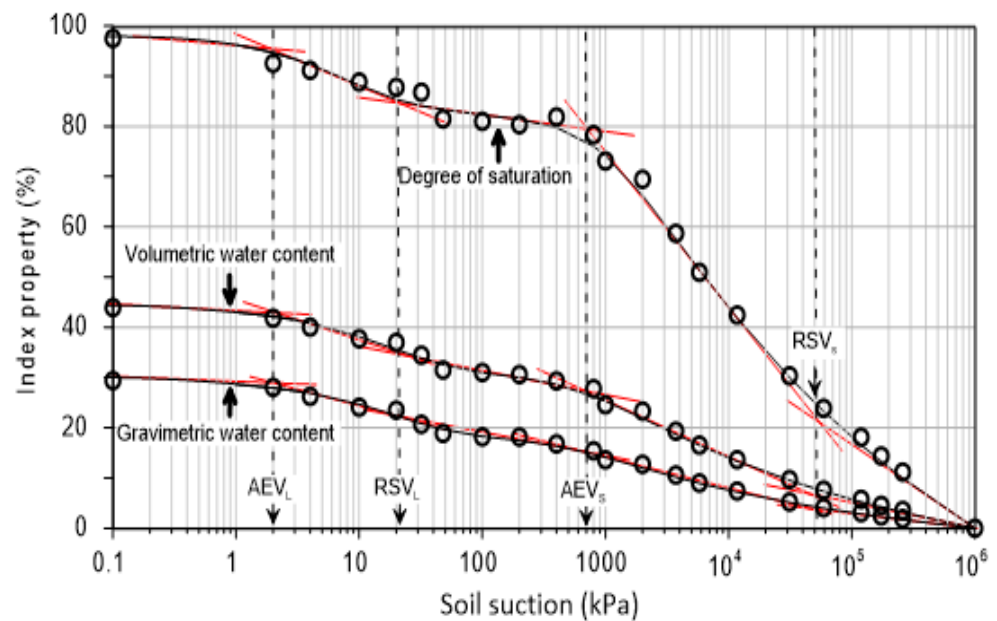


Figure 5. Water retention curve of the investigated clay till.

In the above equation, w_s (30%) is saturated water content, and s (0.37) is related to volumetric ratio of larger pores to all pore sizes. The fitting parameters related to larger pores are a (525), n (−0.85), and m (45), whereas those related to smaller pores are j (500), k (−1.25), and l (0.45).

All the fits showed two air entry values (AEV) and two residual suction values (RSV). This is attributed to the compacted state of soil and is close to the results of a similar till (with $w = 13\%$, $\gamma_d = 17 \text{ kN/m}^3$), as reported by Vanapalli et al. [62]. Compacted soils are characterized by the presence of sub-millimeter size and irregular shapes of lumps (collection of soil particles due to water adsorption [63]), such that the larger pores (pore spaces between the lumps) have more than a 0.1 μm radius, while smaller pores (pores within the lumps) have less than a 0.1 μm radius [64–66]. Furthermore, the number of large pores is comparatively larger than the small pores [67]. This means that the numerous larger pores easily released most of the capillary water at low suction values thereby governing the initial portion of the curve from 0.1 kPa to 700 kPa. Conversely, the fewer

smaller pores released the remainder of capillary water and part of the adsorbed water only with the application of high suction values, that is, in the range of 700 kPa to 10^6 kPa [68].

Irrespective of the index property on the y -axis, the WRC comprised two air entry values and two residual suction values associated with capillary water drainage [69,70]: from larger pores ($AEV_L = 2$ kPa and $RSV_L = 20$ kPa) and from smaller pores ($AEV_S = 700$ kPa and $RSV_S = 5 \times 10^4$ kPa). Beyond RSV_S , vapor flow is dominant until complete dry conditions at 10^6 kPa [71], such that the adsorbed water is removed by evaporation [11]. Furthermore, the plastic limit ($w = 15\%$, $\theta = 30\%$ and $S = 75\%$) was found to match AEV_S , because drainage of capillary water through smaller pores ceases when no more contraction can occur [72]. The various types of WRC have their respective utilities: w -based is most accurate because it is directly measured, θ -based is useful for the determination of water storage capacity, and S -based is the most clear in depicting soil behavior. However, none of these curves can capture volumetric changes due to capillary water through soil pores and adsorbed water on clay particles within lumps [73].

4.4. Volumetric Changes

Figure 6 illustrates the SC with the various S lines were plotted using phase relationships and a G_s of 2.72. The test data was found to best fit the following equation:

$$e = e_d + \frac{e_s - e_d}{1 + b \exp^{-cw}} \tag{2}$$

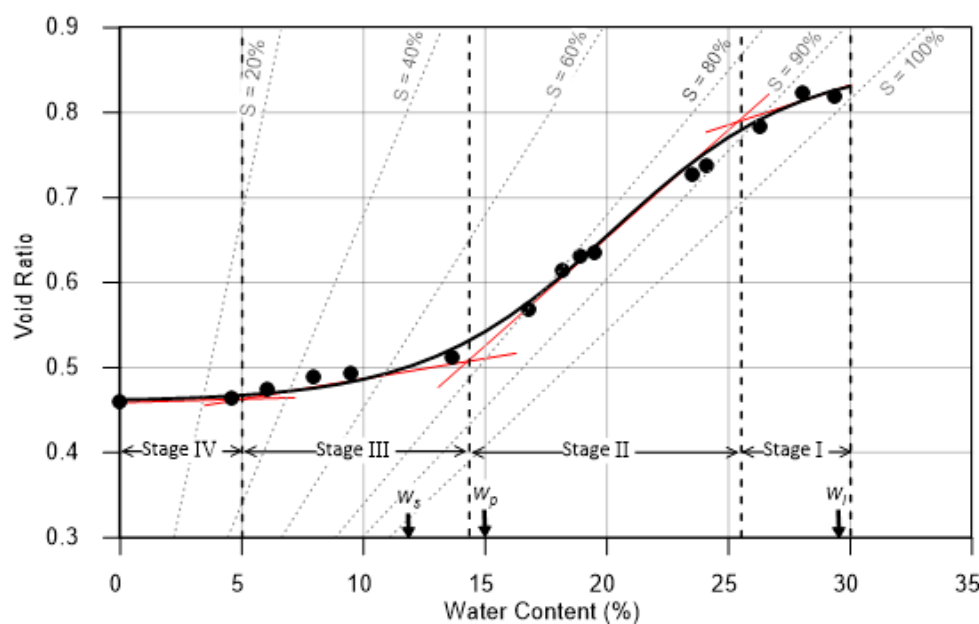


Figure 6. Void ratio versus water content for the investigated clay till.

In the above equation, e_d (0.46) is the void ratio under completely dry conditions, and e_s (0.82) is the saturated void ratio. Likewise, the fitting parameters related to the transition points ($w = 26\%$ and $w = 14\%$) are b (350) and c (29.5).

The shrinkage path of an initially saturated sample followed an s-shaped curve consisting of the following stages [74–76]. Table 3 describes the shrinkage path in terms of e , w , θ and S highlighting the ratio of soil volume change to water volume change (R): stage I ($R = 0.4$), water from most large pores between the lumps was removed with low soil volume change; stage II ($R = 0.8$), water from the remaining larger pores and most of the smaller pores within the lumps was removed with an almost equal value of soil volume change; stage III ($R = 0.3$), water from some of the smaller pores within the lumps were released with low soil volume change; and stage IV ($R = 0.0$), water from the

remaining smaller pores within the lumps was drained with no change in soil volume. The data indicate that about 90% of volume change in the soil occurred in the plastic zone (from liquid limit of 29% to shrinkage limit of 12%) with a change in *S* from 100% to 60% and negligible thereafter, albeit a change in *S* from 60% to 0. Given the deformable nature of the investigated clay till, *SC* must be determined to correlate flow through with volumetric changes.

Table 3. Various stages along the shrinkage path.

Stage	<i>w</i> Range (%)	<i>e</i> Range	θ Range (%)	<i>R</i> *	<i>S</i> Range (%)
I	30–26	0.82–0.79	45–40	0.4	100–90
II	26–14	0.79–0.51	40–24	0.8	90–70
III	14–5	0.51–0.47	24–9	0.3	70–30
IV	5–0	0.47–0.47	9–0	0.0	30–0

* Soil volume change divided by water volume change.

Figure 7 shows swelling potential (change in height with respect to the initial height) versus time. The transient behavior followed an s-shaped curve, comprising an initial swelling (up to 0.3% in 10 min), primary swelling (up to 1.6% in 70 min), and secondary swelling (up to 2.5% in 18 days). During initial swelling, water entered through the larger pores and initiated the expansion of peripheral clay particles of the lumps. The H^+ in the dipolar water molecules were attracted to the net negatively charged clay surfaces, whereas the O^{2-} were pushed away. This generated a gradient that facilitated additional water flow into the pores, thereby increasing the thickness of the diffuse double layer [77]. During primary swelling, water gradually moved from the larger pores into the smaller pores within the lumps. Expansion occurred because the repulsive forces (diffuse double layers between adjacent clay particles in the lumps) exceeded the van der Waals’ attractive forces due to fluctuating dipole–dipole bonds [10,78]. During secondary swelling, expansion of the few remaining clay particles within lumps occurred due to the slow movement of water in the smaller pores. The low swelling potential is attributed to the expansion of clay particles within the larger pores that could not be observed in the vertical direction [79]. Therefore, the transient swelling behavior comprises combined water flow through soil pores and expansion of water film on clay particles in the lumps.

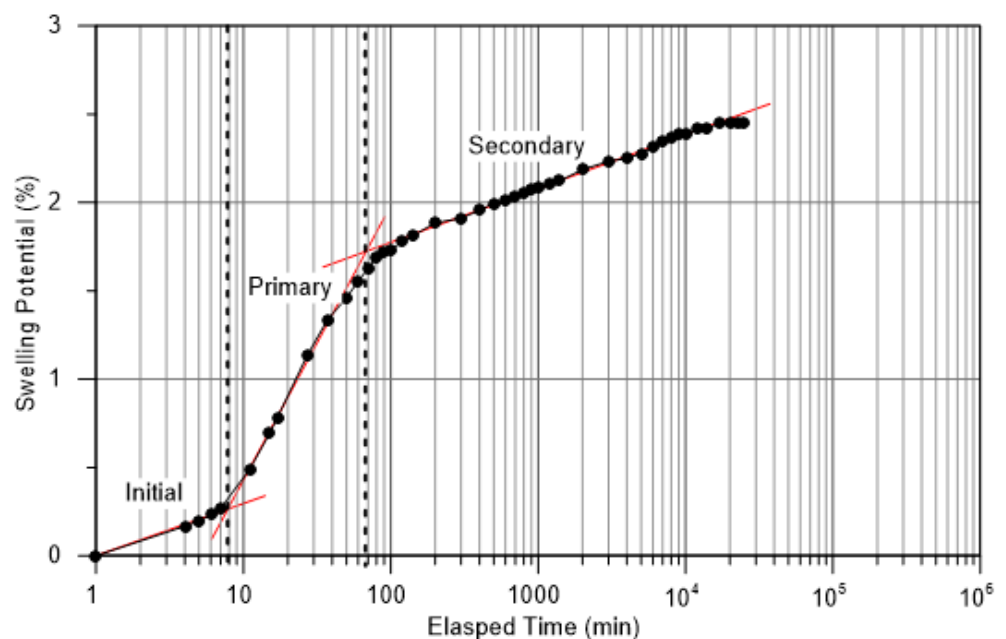


Figure 7. Swelling potential versus time for the investigated clay till.

Figure 8 plots the swelling-consolidation test results. The e increased from 0.55 to 0.59 during swelling, followed by a decrease to 0.27 during consolidation, and then increased to 0.39 during rebound. The compression index (C_c) was calculated to be 0.164, and the rebound index (C_s) was found to be 0.047. These data fall within the ranges of 0.08–0.26 and 0.03–0.09, respectively [3,80]. The low swelling potential (2.5%) under the seating stress (5 kPa) is attributed to the presence of numerous larger pores, which consumed clay expansion in all directions between the lumps. Further decrease in e under applied stresses is attributed to the gradual reduction in the number of large pores and the expulsion of water and air from these pores [68,81]. The adjacent particles slipped due to the presence of water, thereby resulting in re-arrangement of soil particles and reduced pore space. At the end of the test, S was found to be 100% (at $w = 15\%$ and $\gamma_d = 19 \text{ kN/m}^3$), pertaining to the complete air removal during consolidation [82]. The rebound curve is predominantly governed by water adsorption on clay particle surfaces with part of the deformations recovered [83].

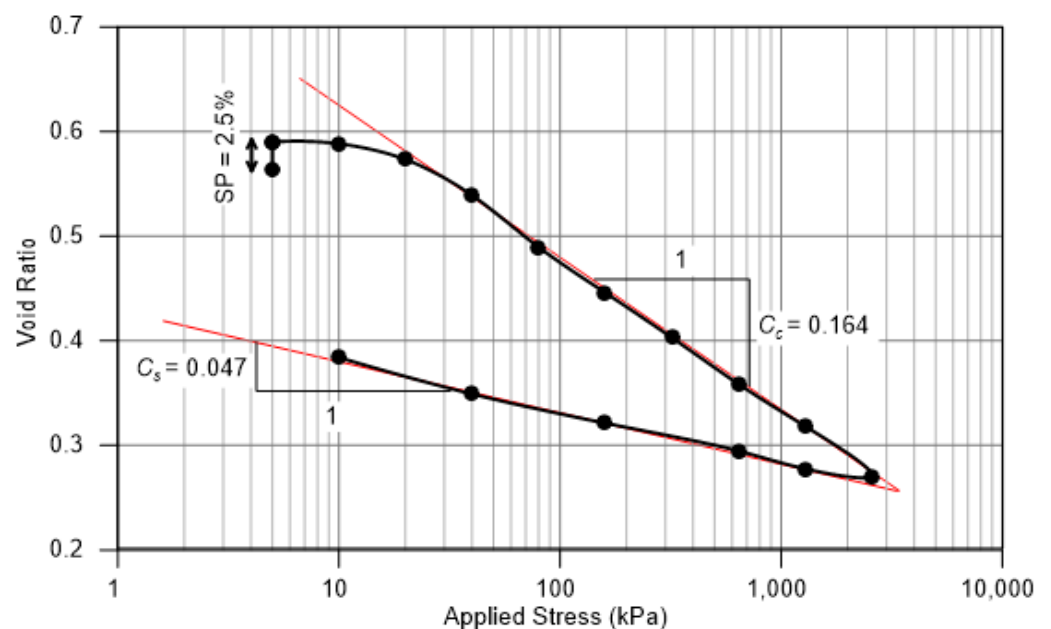


Figure 8. Swell-consolidation test results for the investigated clay till.

4.5. Hydraulic Conductivity

Figure 9 plots the variation of saturated hydraulic conductivity with respect to the void ratio and applied stress. The k_s decreased by three orders of magnitude from $8 \times 10^{-9} \text{ m/s}$ to $8 \times 10^{-12} \text{ m/s}$ when e reduced from 0.59 to 0.27, as the applied stress increased from 10 kPa to about 2600 kPa. The decrease in k_s is attributed to size reduction in large pores that brought the soil particles closer and an increase in resistance to water flow [84]. The data scatter at high e (low applied stress) is associated with the presence of entrapped air in the compacted soil sample [85]. The k_s values were close to the results of similar tills ($k_s = 10^{-9} \text{ m/s}$ to 10^{-11} m/s) reported by Ferris et al. [2] and Vanapalli et al. [62].

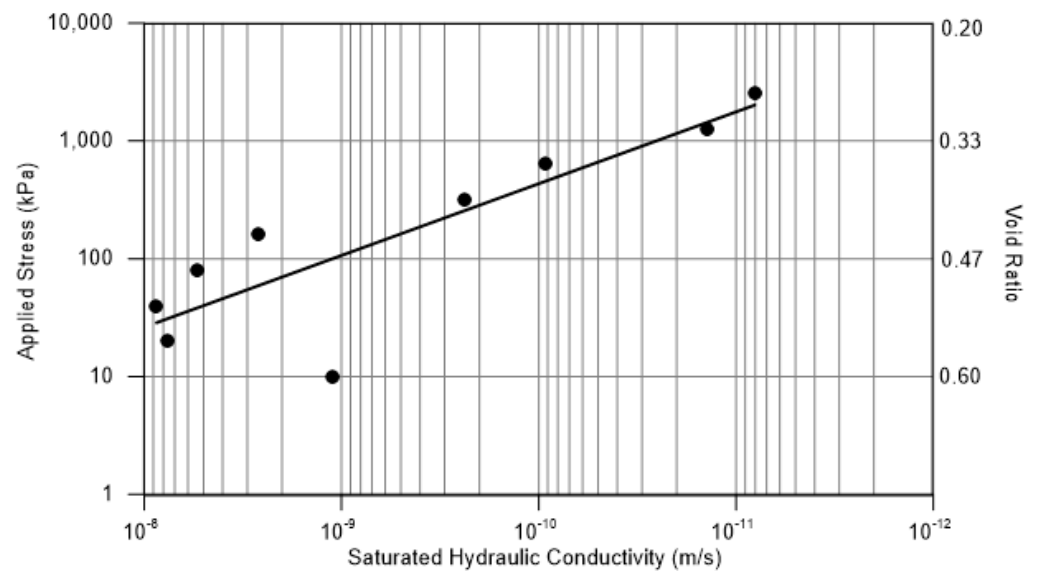


Figure 9. Variation of saturated hydraulic conductivity with void ratio and applied stress for the investigated clay till.

Figure 10 shows the estimated HCC of the clay till using a logarithmic scale and starting at the median k_s value (5×10^{-10} m/s). The HCC was estimated using the modified equation [86]:

$$k_u = k_s \left[\left\{ \frac{s}{\left(\ln \left[2.718 + \left(\frac{a}{\psi} \right)^n \right] \right)^m} + \frac{1-s}{\left(\ln \left[2.718 + \left(\frac{j}{\psi} \right)^k \right] \right)^l} \right\} \left\{ 1 - \frac{\ln \left(1 + \frac{\psi}{3000} \right)}{5.812} \right\} \right]^p \quad (3)$$

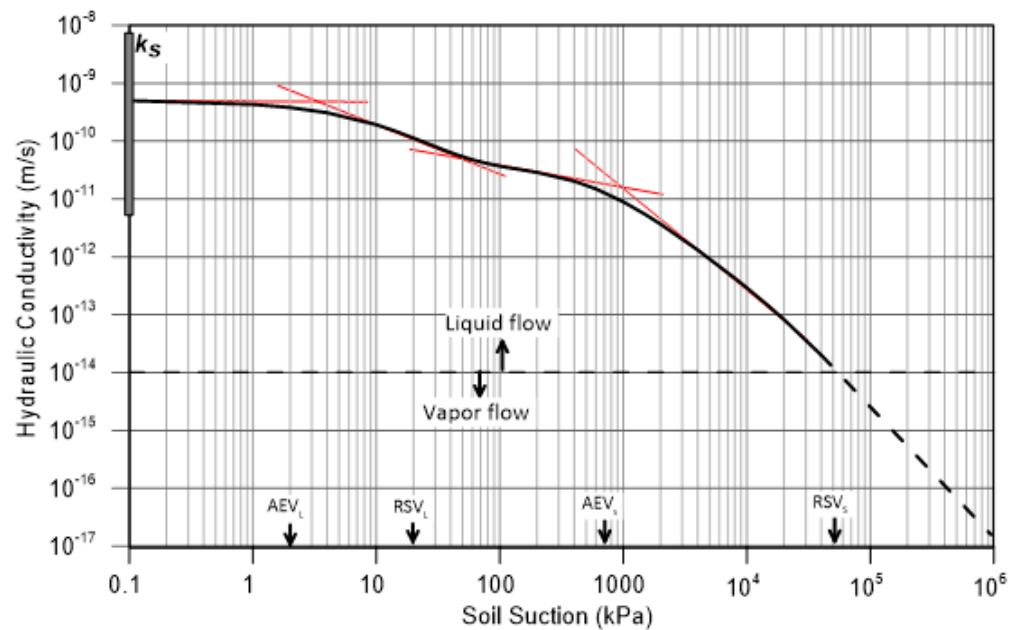


Figure 10. Estimated hydraulic conductivity curve for the investigated clay till.

In the above equation, k_u is the unsaturated hydraulic conductivity, and p (5.5) is the fitting parameter associated with typical hydraulic conductivity curve for clayey soils along with identical WRC parameters (a , n , m , j , k , and l) for the two pore sizes. Based

on statistical analyses of the p parameter for a wide range of soils, the bimodal HCC is considered to accurately represent the behavior of clays [87,88].

The estimated HCC closely followed the bimodal WRC transition points. The k_u remained constant at 5×10^{-10} m/s up to AEV_L and decreased to 8×10^{-11} m/s at RSV_L . Thereafter, k_u slightly decreased to 2×10^{-11} m/s at AEV_S and then significantly decrease to 10^{-14} m/s at RSV_S . The low initial k_u decrease is associated with discontinuous water flow and increased tortuosity between the lumps [69], whereas the final significant k_u decrease is mainly attributed to water flow within the lumps only and may not be continuous across the lumps [70]. Beyond RSV_S , flow occurs in vapor form due to evaporation of adsorbed water from clay particles within the lumps [11].

The HCC correlates well with the observed SP stages, that is, slow rate of initial swelling around $k_u = 10^{-14}$ m/s (RSV_S), significant high rate of primary swelling due to an increasing k_u reaching up to 10^{-11} m/s (AEV_S), and slow rate of secondary swelling under slight k_u increase around 10^{-10} m/s (AEV_L). The low k_u over the entire process resulted in an 18 days test required to fully develop the SP. Finally, and as discussed earlier, the rate of consolidation is related to k_s , which was found to decrease with applied stress.

5. Summary and Conclusions

Glacial geology, marine environment, and arid climate govern the composition and behavior of clay tills. The primary contribution of this research is the conceptual understanding of engineering behavior under two independent state variables of soil suction and applied stress. The effect of soil and water composition on water retention, volume changes, and hydraulic conductivity was investigated. The main conclusions of this paper are given as follows.

The investigated clay till showed moderate water adsorption capacity ($w_l = 29\%$ and $w_p = 15\%$) due to the presence of minerals such as corrensite (26%), illite (10%), and kaolinite (8%), which resulted in a CEC of 26.5 cmol(+)/kg with Ca^{2+} as the dominant cation. The pore water was slightly basic (pH = 7.5), and the ESP (0.75%) indicated a flocculated fabric.

The WRC comprised four transition points associated with capillary water drainage from larger pores ($AEV_L = 2$ kPa and $RSV_L = 20$ kPa) and from smaller pores ($AEV_S = 700$ kPa and $RSV_S = 5 \times 10^4$ kPa). Beyond RSV_S , vapor flow is dominant until 10^6 kPa, such that the adsorbed water is removed by evaporation.

The ratio of soil volume change to water volume change best described the s-shaped shrinkage path. The curve showed drainage from most large pores with low volume change; from the remaining large and most of the small pores with almost equal volume change; from some small pores with low volume change; and from the rest of the small pores with no volume change.

The s-shaped SP curve comprised three stages and correlated well with bimodal HCC: slow initial swelling (k_u around 10^{-14} m/s) due to expansion of peripheral clay in lumps; high primary swelling rate (k_u up to 10^{-11} m/s) due to increased double layer thickness on clay; and slow secondary swelling rate (albeit k_u around 10^{-10} m/s) due to expansion of remaining particles.

Soil compression ($C_c = 0.164$) was due to a gradual reduction in number of larger pores, whereas the rebound ($C_s = 0.047$) was due to water adsorption on clay particles with part of the deformations recovered. Finally, the consolidation rate is related to k_s that varied from 8×10^{-9} m/s to 8×10^{-12} m/s with an applied stress increase from 10 kPa to 2600 kPa.

The correlation of soil and pore water compositions with the engineering behavior of earth structures is crucial in the initial design for new construction and long-term monitoring of constructed facilities. This comprehensive research provides a clear understanding of the saturated and unsaturated soil properties of clay tills.

Author Contributions: Conceptualization, S.A.; Data curation, R.P.; Formal analysis, R.P.; Funding acquisition, S.A.; Investigation, R.P.; Supervision, S.A.; Writing—original draft, R.P.; Writing—review & editing, S.A. All authors have read and agreed to the published version of the manuscript.

Funding: This research was funded by Natural Sciences and Engineering Research Council of Canada, grant number RGPIN-06456-2018.

Data Availability Statement: The data presented in this study are available in the figures and tables.

Acknowledgments: The authors would like to acknowledge the financial assistance provided by Natural Sciences and Engineering Research Council of Canada. Thanks to the University of Regina for providing laboratory space and computing facilities.

Conflicts of Interest: The authors declare no conflict of interest.

References

1. Chen, L.L.; Zhou, G.G.; Mu, Q.Y.; Cui, K.F.E.; Song, D.R. Compression characteristics of saturated re-compacted glacial tills in Tianmo Gully of Tibet, China. *J. Mt. Sci.* **2019**, *16*, 1661–1674. [[CrossRef](#)]
2. Ferris, D.M.; Potter, G.; Ferguson, G. Characterization of the hydraulic conductivity of glacial till aquitards. *Hydrogeol. J.* **2020**, *28*, 1827–1839. [[CrossRef](#)]
3. Sauer, E.K.; Egeland, A.K.; Christiansen, E.A. Compression characteristics and index properties of tills and intertill clays in southern Saskatchewan, Canada. *Can. Geotech. J.* **1993**, *30*, 257–275. [[CrossRef](#)]
4. Quinn, J.; Chin, B.; Pernito, M.; Scammell, J. Geotechnical assessment of the Alameda dam. *Bull. Can. Dam Assoc.* **2015**, *26*, 10–23.
5. Errecalde, I.A. Modelling the SM-3 Dam, Quebec, Canada. Master's Thesis, Polytechnic University of Catalonia, Barcelona, Spain, 2012.
6. Clarke, D.; Smethurst, J.A. Effects of climate change on cycles of wetting and drying in engineered clay slopes in England. *Q. J. Eng. Geol. Hydrogeol.* **2010**, *43*, 473–486. [[CrossRef](#)]
7. Hudacsek, P.; Leung, A. Physical and Numerical Modelling of Climate-Change Influenced, Poorly-Compacted Glacial Till Embankments. In *Geotechnical Engineering for Infrastructure and Development*; ICE Publishing: London, UK, 2015; pp. 3911–3916.
8. Bell, F.G. The geotechnical properties of some till deposits occurring along the coastal areas of eastern England. *Eng. Geol.* **2002**, *63*, 49–68. [[CrossRef](#)]
9. Cao, L.; Peaker, S.; Ahmad, S. A Case Study of Embankment Retaining Wall in Ontario. In Proceedings of the 69th Canadian Geotechnical Conference—GeoVancouver 2016, Vancouver, BC, Canada, 3–5 October 2016.
10. Mitchell, J.K.; Soga, K. *Fundamentals of Soil Behavior*; John Wiley & Sons, Inc.: New York, NY, USA, 2005.
11. Lu, N.; Khorshidi, M. Mechanisms for soil-water retention and hysteresis at high suction range. *J. Geotech. Geoenviron. Eng.* **2015**, *141*, 1–10. [[CrossRef](#)]
12. Zhang, Z.F. Soil water retention and relative permeability for conditions from oven-dry to full saturation. *Vadose Zone J.* **2011**, *10*, 1299–1308. [[CrossRef](#)]
13. Hillel, D. *Environmental Soil Physics: Fundamentals, Applications, and Environmental Considerations*; Academic Press: San Diego, CA, USA, 1998.
14. Tokunaga, T.K. Hydraulic properties of adsorbed water films in unsaturated porous media. *Water Resour. Res.* **2009**, *45*. [[CrossRef](#)]
15. Schanz, T.; Tripathy, S. Swelling pressure of a divalent-rich bentonite: Diffuse double-layer theory revisited. *Water Resour. Res.* **2009**, *45*. [[CrossRef](#)]
16. Gao, C. Theory of menisci and its applications. *Appl. Phys. Lett.* **1997**, *71*, 1801–1803. [[CrossRef](#)]
17. Lu, N. Generalized soil water retention equation for adsorption and capillarity. *J. Geotech. Geoenviron. Eng.* **2016**, *142*. [[CrossRef](#)]
18. Or, D.; Tuller, M. Liquid retention and interfacial area in variably saturated porous media: Upscaling from single-pore to sample-scale model. *Water Resour. Res.* **1999**, *35*, 3591–3605. [[CrossRef](#)]
19. Lu, N.; Dong, Y. Correlation between soil-shrinkage curve and water-retention characteristics. *J. Geotech. Geoenviron. Eng.* **2017**, *143*. [[CrossRef](#)]
20. Zhou, A.; Wu, S.; Li, J.; Sheng, D. Including degree of capillary saturation into constitutive modelling of unsaturated soils. *Comput. Geotech.* **2018**, *95*, 82–98. [[CrossRef](#)]
21. Acton, D.F.; Padbury, G.A.; Stushnoff, C.T. *The Eco-Regions of Saskatchewan*; Hignell: Winnipeg, MB, Canada, 1998.
22. Ito, M.; Azam, S. Engineering characteristics of a glacio-lacustrine clay deposit in a semi-arid climate. *Bull. Eng. Geol. Environ.* **2009**, *68*, 551. [[CrossRef](#)]
23. Vonhof, J.A. Tertiary Gravels and Sands in the Canadian Great Plains. Ph.D. Thesis, University of Saskatchewan, Saskatoon, SK, Canada, 1969.
24. Scott, J.S.; Brooker, E.W. *Geological and Engineering Aspects of Upper Cretaceous Shale in Western Canada*; Geological Survey of Canada: Ottawa, ON, Canada, 1968.
25. Dawson, F.M.; Evans, C.G.; Marsh, R.; Richardson, R. Uppermost Cretaceous and Tertiary Strata of the Western Canada Sedimentary Basin. In *Geological Atlas of the Western Canada Sedimentary Basin*; Alberta Research Council: Calgary, AB, Canada, 1994.

26. Street, H.P.; Bamforth, E.L.; Gilbert, M.M. The formation of a Marine Bonebed at the Upper Cretaceous Dinosaur Park–Bearpaw transition of west-central Saskatchewan, Canada. *Front. Earth Sci.* **2019**, *7*, 209. [[CrossRef](#)]
27. Stalker, A.M. Identification of Saskatchewan gravels and sands. *Can. J. Earth Sci.* **1968**, *5*, 155–163. [[CrossRef](#)]
28. Holman, J.A. Climatic significance of giant tortoises from the Wood Mountain Formation (upper Miocene) of Saskatchewan. *Can. J. Earth Sci.* **1971**, *8*, 1148–1151. [[CrossRef](#)]
29. Wolfe, J.A.; Upchurch, G.R., Jr. North American nonmarine climates and vegetation during the Late Cretaceous. *Palaeogeogr. Palaeoclimatol. Palaeoecol.* **1987**, *61*, 33–77. [[CrossRef](#)]
30. Weaver, C.E. Clays, Muds, and Shales. In *Developments in Sedimentology*; Elsevier: New York, NY, USA, 1989; Volume 44.
31. Christiansen, E.A. Tills in Southern Saskatchewan, Canada. In *Till, a Symposium*; Ohio State University Press: Columbus, OH, USA, 1971; pp. 167–183.
32. Hanson, M.A. South Tantalito Quaternary Project: Surficial Geology and Drift Prospecting Potential of the Southern Tantalito Domain, Saskatchewan. In *Summary of Investigations 2016, Saskatchewan Geological Survey*; Miscellaneous Report 2016-4.2; Saskatchewan Ministry of the Economy: Regina, SK, Canada, 2016.
33. Christiansen, E.A. The Wisconsinan deglaciation of southern Saskatchewan and adjacent areas. *Can. J. Earth Sci.* **1979**, *16*, 913–938. [[CrossRef](#)]
34. Sauchyn, D.J. A reconstruction of Holocene geomorphology and climate, western Cypress Hills, Alberta and Saskatchewan. *Can. J. Earth Sci.* **1990**, *27*, 1504–1510. [[CrossRef](#)]
35. Sauer, E.K.; Egeland, A.K.; Christiansen, E.A. Preconsolidation of tills and intertill clays by glacial loading in southern Saskatchewan, Canada. *Can. J. Earth Sci.* **1993**, *30*, 420–433. [[CrossRef](#)]
36. Cassagrande, A. Classification and identification of soils. *Trans. Am. Soc. Civ. Eng.* **1948**, *113*, 901–930. [[CrossRef](#)]
37. Holtz, R.D.; Kovacs, W.D. *An Introduction to Geotechnical Engineering*; Prentice-Hall, Inc.: Englewood Cliffs, NJ, USA, 1981.
38. American Society for Testing and Materials. Standard Practices for Preserving and Transporting Soil Samples. In *Annual Book of ASTM Standards*; ASTM D4220/D4220M-14; American Society for Testing and Materials: West Conshohocken, PA, USA, 2014.
39. American Society for Testing and Materials. Standard Test Methods for Specific Gravity of Soil Solids by Water Pycnometer. In *Annual Book of ASTM Standards*; ASTM D854-14; American Society for Testing and Materials: West Conshohocken, PA, USA, 2014.
40. American Society for Testing and Materials. Standard Test Method for Particle-Size Analysis of Soils (Withdrawn 2016). In *Annual Book of ASTM Standards*; ASTM D422-63(2007)e2; American Society for Testing and Materials: West Conshohocken, PA, USA, 2007.
41. American Society for Testing and Materials. Standard Test Methods for Liquid Limit, Plastic Limit, and Plasticity Index of Soils. In *Annual Book of ASTM Standards*; ASTM D4318-17e1; American Society for Testing and Materials: West Conshohocken, PA, USA, 2017.
42. American Society for Testing and Materials. Standard Practice for Classification of Soils for Engineering Purposes (Unified Soil Classification System). In *Annual Book of ASTM Standards*; ASTM D2487-17e1; American Society for Testing and Materials: West Conshohocken, PA, USA, 2017.
43. American Society for Testing and Materials. Standard Test Methods for Laboratory Determination of Water (Moisture) Content of Soil and Rock by Mass. In *Annual Book of ASTM Standards*; ASTM D2216-19; American Society for Testing and Materials: West Conshohocken, PA, USA, 2019.
44. Hubbard, C.R.; Snyder, R.L. RIR-measurement and use in quantitative XRD. *Powder Diffr.* **1988**, *3*, 74–77. [[CrossRef](#)]
45. Hendershot, W.H.; Lalonde, H.; Duquette, M. Ion Exchange and Exchangeable Cations. In *Soil Sampling and Methods of Analysis*; Carter, M.R., Ed.; CRC Press: Boca Raton, FL, USA, 2008.
46. American Society for Testing and Materials. Standard Test Methods for pH of Soils. In *Annual Book of ASTM Standards*; ASTM D4972-19; American Society for Testing and Materials: West Conshohocken, PA, USA, 2019.
47. American Society for Testing and Materials. Standard Test Methods for Electrical Conductivity and Resistivity of Water. In *Annual Book of ASTM Standards*; ASTM D1125-14; American Society for Testing and Materials: West Conshohocken, PA, USA, 2014.
48. Azam, S.; Rima, U.S. Oil sand tailings characterisation for centrifuge dewatering. *Environ. Geotech.* **2014**, *1*, 189–196. [[CrossRef](#)]
49. American Society for Testing and Materials. Standard Test Methods for Laboratory Compaction Characteristics of Soil Using Standard Effort (12 400 ft-lbf/ft³ (600 kN-m/m³)). In *Annual Book of ASTM Standards*; ASTM D698-12e2; American Society for Testing and Materials: West Conshohocken, PA, USA, 2012.
50. American Society for Testing and Materials. Standard Test Methods for Determination of the Soil Water Characteristic Curve for Desorption Using Hanging Column, Pressure Extractor, Chilled Mirror Hygrometer, or Centrifuge. In *Annual Book of ASTM Standards*; ASTM D6836-16; American Society for Testing and Materials: West Conshohocken, PA, USA, 2016.
51. American Society for Testing and Materials. Standard Test Method for Shrinkage Factors of Cohesive Soils by the Water Submersion Method. In *Annual Book of ASTM Standards*; ASTM D4943-18; American Society for Testing and Materials: West Conshohocken, PA, USA, 2018.
52. American Society for Testing and Materials. Standard Test Methods for One-Dimensional Swell or Collapse of Soils. In *Annual Book of ASTM Standards*; ASTM D4546-14e1; American Society for Testing and Materials: West Conshohocken, PA, USA, 2014.

53. American Society for Testing and Materials. Standard Test Methods for One-Dimensional Consolidation Properties of Soils Using Incremental Loading. In *Annual Book of ASTM Standards*; ASTM D2435/D2435M-11(2020); American Society for Testing and Materials: West Conshohocken, PA, USA, 2020.
54. Terzaghi, K.; Peck, R.B.; Mesri, G. *Soil Mechanics in Engineering Practice*; John Wiley & Sons Inc.: New York, NY, USA, 1996.
55. Ellis, J.G.; Acton, D.F.; Moss, H.C. *The Soils of the Willow Bunch Lake Map Area (72H) Saskatchewan*; Saskatchewan Institute of Pedology: Saskatoon, SK, Canada, 1967.
56. Braman, D.R.; Sweet, A.R.; Lerbekmo, J.F. Upper Cretaceous-lower Tertiary lithostratigraphic relationships of three cores from Alberta, Saskatchewan, and Manitoba, Canada. *Can. J. Earth Sci.* **1999**, *36*, 669–683. [[CrossRef](#)]
57. Środoń, J. Nature of mixed-layer clays and mechanisms of their formation and alteration. *Annu. Rev. Earth Planet. Sci.* **1999**, *27*, 19–53. [[CrossRef](#)]
58. Wilson, M.J.; Deer, W.A.; Howie, R.A.; Zussman, J. *Rock-Forming Minerals, Sheet Silicates: Clay Minerals*; Geological Society of London: London, UK, 2013; Volume 3C.
59. Azam, S. Effect of composition and morphology on self-weight settling of laterite ore slurries. *Geotech. Geol. Eng.* **2012**, *30*, 107–118. [[CrossRef](#)]
60. Chorom, M.; Rengasamy, P. Dispersion and zeta potential of pure clays as related to net particle charge under varying pH, electrolyte concentration and cation type. *Eur. J. Soil Sci.* **1995**, *46*, 657–665. [[CrossRef](#)]
61. Fredlund, M.D. The Role of Unsaturated Soil Property Functions in the Practice of Unsaturated Soil Mechanics. Ph.D. Thesis, University of Saskatchewan, Saskatoon, SK, Canada, 2000.
62. Vanapalli, S.K.; Fredlund, D.G.; Pufahl, D.E. Comparison of Saturated-Unsaturated Shear Strength and Hydraulic Conductivity Behavior of a Compacted Sandy-Clay Till. In Proceedings of the 50th Canadian Geotechnical Conference, Ottawa, ON, Canada, 20–22 October 1997; pp. 625–632.
63. Menon, M.; Yuan, Q.; Jia, X.; Dougill, A.J.; Hoon, S.R.; Thomas, A.D.; Williams, R.A. Assessment of physical and hydrological properties of biological soil crusts using X-ray microtomography and modeling. *J. Hydrol.* **2011**, *397*, 47–54. [[CrossRef](#)]
64. Collins, K.; McGown, A. The form and function of microfabric features in a variety of natural soils. *Geotechnique* **1974**, *24*, 233–254. [[CrossRef](#)]
65. Simms, P.H.; Yanful, E.K. Measurement and estimation of pore shrinkage and pore distribution in a clayey till during soil-water characteristic curve tests. *Can. Geotech. J.* **2001**, *38*, 741–754. [[CrossRef](#)]
66. Najser, J.; Pooley, E.; Springman, S.M.; Laue, J.; Boháč, J. Mechanisms controlling the behaviour of double-porosity clay fills in situ and centrifuge study. *Q. J. Eng. Geol. Hydrogeol.* **2010**, *43*, 207–220. [[CrossRef](#)]
67. Leroueil, S.; Hight, D.W. Compacted Soils: From Physics to Hydraulic and Mechanical Behavior. In Proceedings of the 1st Pan-American Conference on Unsaturated Soils, Cartagena de Indias, Colombia, 19–22 February 2013; Taylor & Francis Group: Boca Raton, FL, USA, 2013; pp. 41–59.
68. Maleksaeedi, E.; Nuth, M. Evaluation of capillary water retention effects on the development of the suction stress characteristic curve. *Can. Geotech. J.* **2019**, *57*, 1439–1452. [[CrossRef](#)]
69. Chen, R.P.; Liu, P.; Liu, X.M.; Wang, P.F.; Kang, X. Pore-scale model for estimating the bimodal soil–water characteristic curve and hydraulic conductivity of compacted soils with different initial densities. *Eng. Geol.* **2019**, *260*, 105199. [[CrossRef](#)]
70. Ito, M.; Azam, S. Relation between flow through and volumetric changes in natural expansive soils. *Eng. Geol.* **2020**, *279*, 105885. [[CrossRef](#)]
71. Ebrahimi-Birang, N.; Gitirana Jr, G.F.N.; Fredlund, D.G.; Fredlund, M.D.; Samarasekera, L. A Lower Limit for the Water Permeability Coefficient. In Proceedings of the 57th Canadian Geotechnical Conference, Quebec City, QC, Canada, 24–26 October 2004; pp. 24–27.
72. Li, X.; Zhang, L.M.; Wu, L.Z. A framework for unifying soil fabric, suction, void ratio, and water content during the dehydration process. *Soil Sci. Soc. Am. J.* **2014**, *78*, 387–399. [[CrossRef](#)]
73. Azam, S.; Chowdhury, R.H. Swell–shrink–consolidation behavior of compacted expansive clays. *Int. J. Geotech. Eng.* **2013**, *7*, 424–430. [[CrossRef](#)]
74. Haines, W.B. The volume changes associated with variations of water content in soil. *J. Agric. Sci.* **1923**, *13*, 296–310. [[CrossRef](#)]
75. Hobbs, P.R.N.; Jones, L.D.; Kirkham, M.P.; Gunn, D.A.; Entwisle, D.C. Shrinkage limit test results and interpretation for clay soils. *Q. J. Eng. Geol. Hydrogeol.* **2019**, *52*, 220–229. [[CrossRef](#)]
76. Stirk, G.B. Some aspects of soil shrinkage and the effect of cracking upon water entry into the soil. *Aust. J. Agric. Res.* **1954**, *5*, 279–291. [[CrossRef](#)]
77. Low, P.F. Interparticle Forces in Clay Suspensions: Flocculation, Viscous Flow, and Swelling. In *Clay-Water Interface and Its Rheological Implications*; CMS Workshop Lectures, Guven, N., Pollastro, R.M., Eds.; The Clay Minerals Society: Boulder, CO, USA, 1992; Volume 4, pp. 158–190.
78. Van Olphen, H. Compaction of clay sediments in the range of molecular particle distances. *Clays Clay Miner.* **1962**, *11*, 178–187. [[CrossRef](#)]
79. Ito, M.; Azam, S. Determination of swelling and shrinkage properties of undisturbed expansive soils. *Geotech. Geol. Eng.* **2010**, *28*, 413–422. [[CrossRef](#)]
80. MacDonald, A.B.; Sauer, E.K. The engineering significance of Pleistocene stratigraphy in the Saskatoon area, Saskatchewan, Canada. *Can. Geotech. J.* **1970**, *7*, 116–126. [[CrossRef](#)]

81. Alonso, E.E.; Pinyol, N.M.; Gens, A. Compacted soil behavior: Initial state, structure, and constitutive modelling. *Geotechnique* **2013**, *63*, 463–478. [[CrossRef](#)]
82. Rahardjo, H.; Fredlund, D.G. Experimental verification of the theory of consolidation for unsaturated soils. *Can. Geotech. J.* **1995**, *32*, 749–766. [[CrossRef](#)]
83. Cui, Y.J.; Nguyen, X.P.; Tang, A.M.; Li, X.L. An insight into the unloading/reloading loops on the compression curve of natural stiff clays. *Appl. Clay Sci.* **2013**, *83–84*, 343–348. [[CrossRef](#)]
84. Romero, E.; Della Vecchia, G.; Jommi, C. An insight into the water retention properties of compacted clayey soils. *Geotechnique* **2011**, *61*, 313–328. [[CrossRef](#)]
85. Olsen, H.W.; Nichols, R.W.; Rice, T.L. Low gradient permeability measurements in triaxial system. *Geotechnique* **1985**, *35*, 145–157. [[CrossRef](#)]
86. Leong, E.C.; Rahardjo, H. Permeability functions for unsaturated soils. *J. Geotech. Geoenviron. Eng.* **1997**, *123*, 1118–1126. [[CrossRef](#)]
87. Fredlund, D.G.; Rahardjo, H.; Fredlund, M.D. *Unsaturated Soil Mechanics in Engineering Practice*; John Wiley & Sons, Inc.: Hoboken, NJ, USA, 2012.
88. Zhai, Q.; Rahardjo, H. Estimation of permeability function from the soil–water characteristic curve. *Eng. Geol.* **2015**, *199*, 148–156. [[CrossRef](#)]